NANO LETTERS

pubs.acs.org/NanoLett

Letter

Quantum Sensing of Opaque Materials with Plasmonically Enhanced Hexagonal Boron Nitride Spin Defects

Saakshi Dikshit, Sumukh Vaidya, Troy Tsubota, Xingyu Gao, Peng Ju, Zhiyan Xie, Kunhong Shen, Naveed Hussain, Shougo Higashi, Debasish Banerjee, Songtao Wu,* and Tongcang Li*

Cite This: *Nano Lett.* 2026, 26, 4410−4417

Read Online

ACCESS | Metrics & More | Article Recommendations | Supporting Information

ABSTRACT: Spin defects in hexagonal boron nitride (hBN) are emerging platforms for quantum sensing. The negatively charged boron vacancy (V_B^-) is widely studied due to its robust spin properties, but its low brightness often requires plasmonic enhancement, limiting sensing in optically opaque or scattering environments, such as batteries. Here, we design and nanofabricate a coplanar waveguide integrated with nanoslit arrays to enable back-side excitation and photoluminescence collection from hBN spin defects. Using a neon focused ion beam, we pattern periodic nanoslits through a thin gold film, allowing simultaneous microwave delivery and optical access through the substrate. We demonstrate device performance via T_1 relaxometry and magnetic field mapping of nickel nanoparticles. This platform enables plasmonically enhanced quantum sensing in opaque materials and liquids, expanding applications beyond conventional transparent systems.

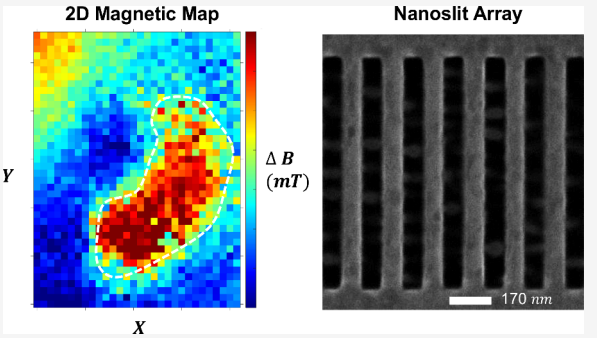

KEYWORDS: *hexagonal boron nitride, quantum sensing, spin defects, 2D materials, plasmonic waveguide*

Spin defects in hexagonal boron nitride (hBN)[1] have emerged as powerful platforms for quantum sensing,[2] with demonstrated applications in sensing static magnetic fields,[3−5] paramagnetic spins,[6,7] strain,[8,9] temperature,[10,11] nuclear spins,[12] magnon dynamics,[13] etc. As a two-dimensional (2D) van der Waals (vdW) material, hBN can be exfoliated into ultrathin flakes, offering unique advantages for nanoscale sensing. The absence of dangling bonds on its surface allows spin defects to preserve spin and optical properties even in close proximity to the surface. Recently, spin defects in few-layer hBN have been employed for sensing magnons in magnetic insulators,[14] significantly reducing the sample−sensor distance and thereby enhancing both spatial resolution and sensitivity. Furthermore, the 2D nature of hBN facilitates integration into heterostructures,[15−17] supporting scalable, low-cost fabrication of hybrid quantum devices.

Among various spin defects in hBN, the negatively charged boron vacancy (V_B^-) is the most widely used one for sensing applications, owing to its robust spin properties and ease of creation. However, a major limitation of the V_B^- defects is its intrinsically low brightness,[18] which hampers optical signal collection and sensing sensitivity. To overcome this challenge, plasmonic enhancement techniques have been widely employed, using either planar gold films or engineered plasmonic nanocavities. These structures amplify the local electromagnetic field near the defect, thereby increasing the spontaneous emission rate and improving the quantum efficiency of the emitter. A variety of plasmonic architectures have been designed to this end, including gold nanotrenches[19] and silver nanocubes[20,21] and nanopillars[8,9] to further enhance the brightness, all of which have demonstrated significant improvements in brightness and, consequently, the sensitivity of V_B^--based spin sensors.

While plasmonically enhanced spin defects in hBN have been used to study various physical quantities, sensing opaque materials remains challenging. In a conventional experimental setup, opaque materials and plasmonic waveguides block much of the hBN photoluminescence (PL) from either direction, limiting optical measurements. Omega-shaped waveguides can be used to sense opaque materials but lack plasmonic enhancement and have less efficient microwave driving, limiting the sensitivity of hBN spin sensors.

Sensing opaque materials plays a key role in studying lithium-ion batteries, which are widely used as rechargeable energy sources.[22,23] Non-destructive techniques that measure stress, magnetic fields, currents, and temperature are crucial for understanding battery performance and extending lifespan. Since important constituents of lithium-ion batteries, such as

Received: January 8, 2026
Revised: March 14, 2026
Accepted: March 20, 2026
Published: March 30, 2026

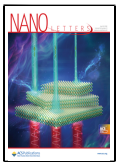

https://doi.org/10.1021/acs.nanolett.6c00108
Nano Lett. 2026, 26, 4410−4417

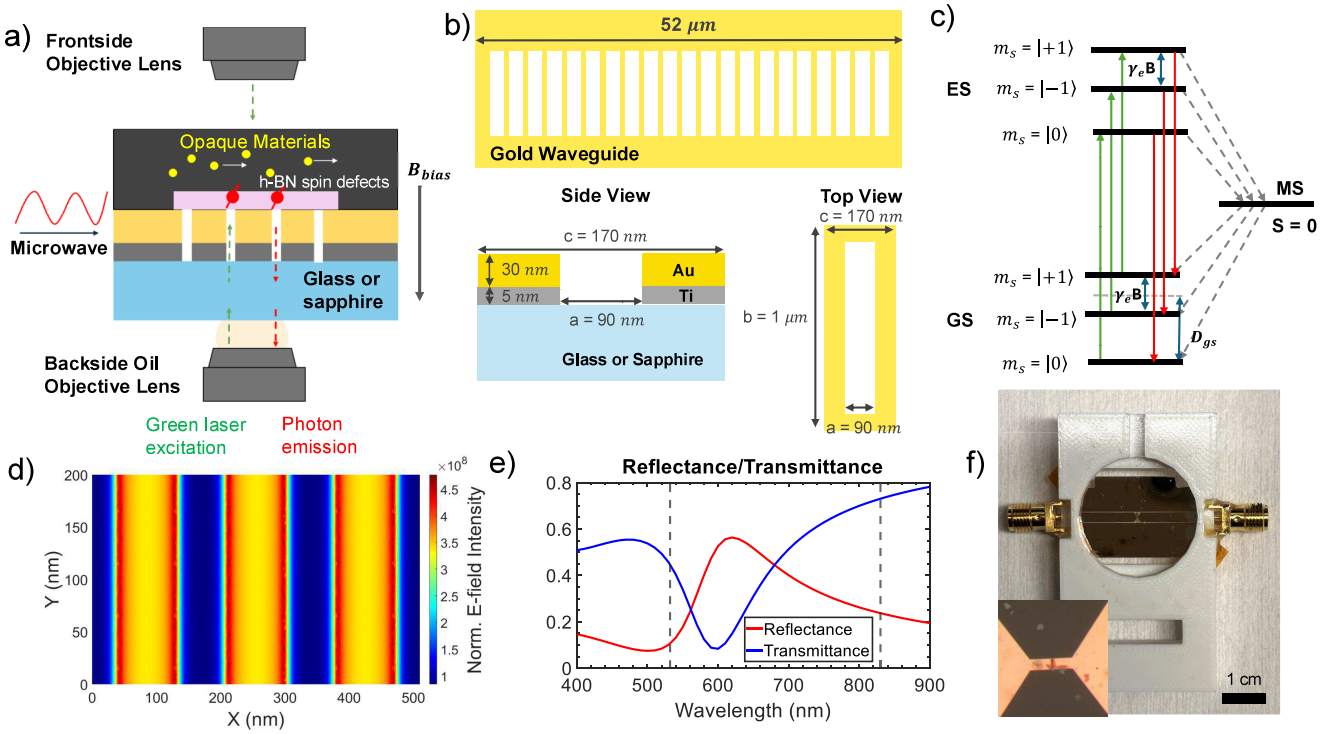

Figure 1. Proposed design for backward sensing of opaque materials using spin defects in hBN. (a) Schematic for the experimental setup. The waveguide consists of a 5 nm film of titanium and 30 nm film of gold fabricated on a 100−150 μm thick silica glass/sapphire coverslip. An oil immersion lens is used to collect photoemission from the backside of the device. (b) Schematic of the top and side views of the proposed nanoslit array. (c) Spin electronic structure of the V_B^- defect. The ground state (GS) and excited state (ES) are spin $S = 1$ systems, with the metastable state (MS) being a singlet $S = 0$ system. Green arrows show 532 nm excitation; red arrows show spin-preserving radiative emission; and gray dotted arrows show spin non-conserving, non-radiative decay via the intersystem crossing (ISC). (d) COMSOL simulations showing the enhanced normalized E-field intensity within the nanoslits. The incident field is x-polarized. (e) Reflectance/transmittance through the nanoslit array for different wavelengths. The gray dashed lines mark the reflectance and transmittance through the nanoslit array at 532 and 830 nm. (f) Picture of the backside of the device. The device is attached to a plastic holder, enabling data collection from both sides. (Inset) Optical image of the microwave stripline.

nickel, cobalt, and manganese, are opaque, these sensing methods are essential for studying the inner workings of lithium-ion batteries.

While various techniques have been utilized to study lithium-ion batteries,[24−30] quantum sensors, such as nitrogen-vacancy (NV) centers in diamond, offer significant advantages in terms of the dynamic range and spatial resolution for studying charge−discharge currents[31−33] and nanoscale electrochemical reactions.[34] Spin defects in van der Waals materials like hexagonal boron nitride (hBN) can offer further advantages by reducing the target-to-sensor separation and offer ease of integrability, with spin defects in thin-film hBN being produced at wafer scales.[35]

In this work, we propose a novel waveguide design that allows us to study the effects of opaque materials using plasmonically enhanced spin defects in hBN. We pattern a plasmonic nanoslit array onto the gold waveguide, which not only enables us to collect light through the backside of the device but also enhances the PL signal from the hBN flakes due to plasmonic enhancement. We demonstrate the capability of this device by performing T_1 spin relaxometry to observe a reduction in the T_1 relaxation time due to magnetic spin noise from nickel nanoparticles and measuring a 2D magnetic map of nickel nanoparticles. This work opens up new avenues for studying opaque materials using hBN.

Figure 1a illustrates our experimental device, which consists of a 30 nm thick gold coplanar waveguide fabricated on a sapphire substrate. An array of nanoslits is patterned into the gold stripline using a neon focused ion beam (FIB), with the dimensions shown in Figure 1b. A hBN flake implanted with V_B^- spin defects is then transferred on top of the nanoslits and serves as the quantum sensor. This device design enables optical excitation and collection of PL from both the front- and backsides using objective lenses, offering flexible optical access.

The hBN V_B^- defect is formed by the absence of a boron atom in the lattice in a negatively charged state. Its electronic structure is shown in Figure 1c.[36−39] The ground state (GS) and excited state (ES) of the V_B^- defect are spin $S = 1$, with the ground state zero field splitting (ZFS) D_{gs} = 3.47 GHz. The spin quantization axis is oriented perpendicular to the plane of the hBN flake. The $m_s = \pm 1$ spin sublevels are non-degenerate in the presence of an externally applied magnetic field along the spin quantization axis due to the Zeeman effect. Optically detected magnetic resonance (ODMR) is enabled by the spin-dependent PL contrast between the $m_s = 0$ and ± 1 states, combined with optical spin polarization into the $m_s = 0$ state under 532 nm laser excitation.

To estimate the plasmonic enhancement provided by the nanoslit structure, we performed finite-element simulations using COMSOL. As seen in Figure 1d, the local electric field intensity at the emission wavelength of V_B^- defects (~830 nm) is enhanced by a factor of ~3.5 within the nanoslit array compared to a flat gold surface. In the simulations, we assumed

https://doi.org/10.1021/acs.nanolett.6c00108
Nano Lett. 2026, 26, 4410−4417

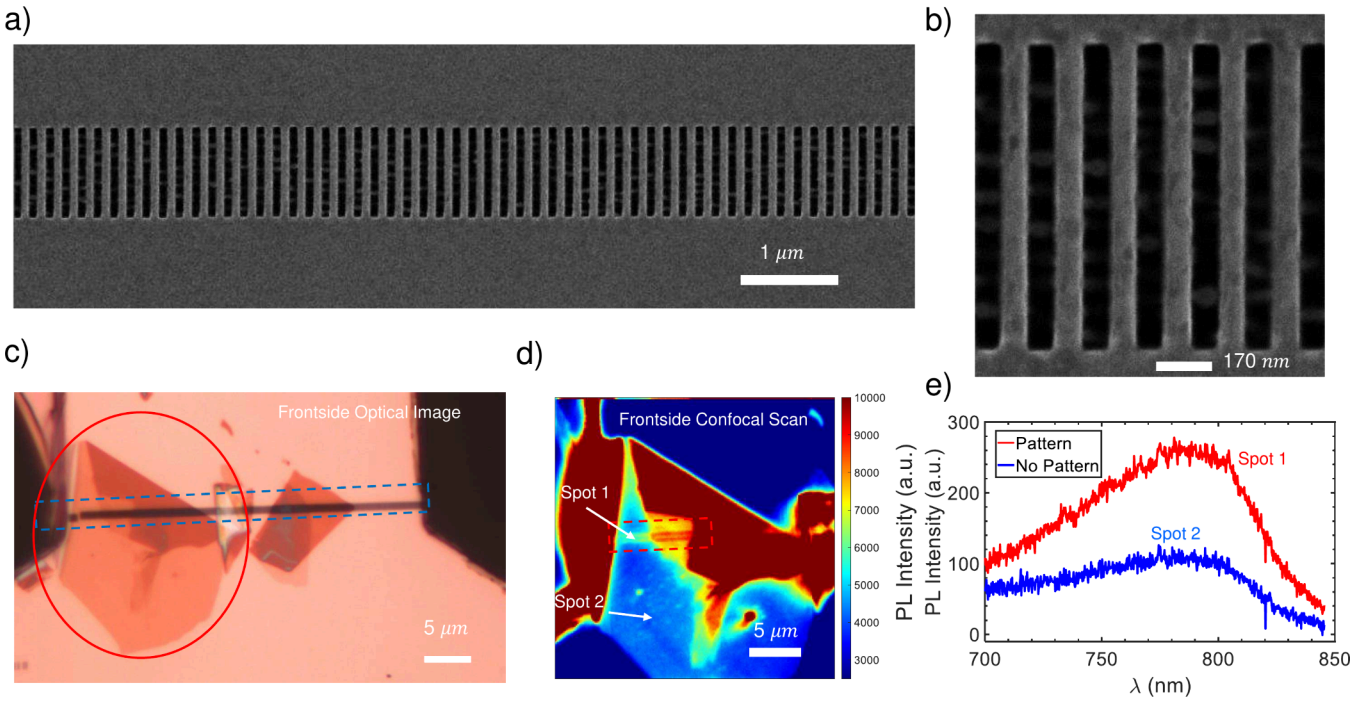

Figure 2. Fabrication of the proposed nanoslit array and plasmonic enhancement of V_B^- defects. (a) Image of the fabricated nanoslit array on gold. The patterning is done using a neon focused ion beam (FIB), whereas the imaging is done using a helium FIB. (b) Close-up image of the nanoslit array showing the nanoscale resolution of the FIB patterning. (c) Optical image of hBN flakes deposited on top of the fabricated gold waveguide. The nanoslit array is highlighted by the dotted blue line. (d) PL confocal of He^+-implanted hBN flakes. The V_B^- defects on the pattern are plasmonically enhanced. The laser power used is 2 mW. (e) PL spectrum of the emission from V_B^- defects on the nanoslit pattern and off the pattern. This shows the enhanced brightness of the defects due to plasmonics in the nanoslit array. The laser power used is 2 mW.

the thickness of the hBN flakes to be 15 nm and the depth of the V_B^- spin defects to be 10 nm from the surface of the hBN flake (Figure 1d and e). Through the COMSOL simulations, we observed that transmission through the nanoslit array is strongly dependent on the width of the nanoslit, namely, a (Figure 1b). However, increasing the nanoslit width while keeping the period c the same leads to a decrease in plasmonic enhancement within the nanoslits. Thus, the nanoslit width a and period c have to be balanced to ensure maximum collection efficiency from the backside of the device. To ensure a highly optimized design, we ran COMSOL simulations, varied the nanoslit width (expressed as a fraction of the period) and the period, and plotted the product of the plasmonic enhancement in the nanoslit and the transmission through the nanoslit (Supplementary Figure 1d). We selected the design with a = 90 nm and c = 170 nm, which is well-optimized for the purpose of collecting maximum PL from the backside.

We attached our sensing device to a 3D-printed plastic holder using epoxy, which enabled us to image the device from both the front- and backsides (Figure 1f). To avoid a loss in the PL signal through the coverslip due to refractive index mismatch, we used an oil immersion lens to excite and collect emission from the V_B^- defects from the backside to study opaque materials deposited on top of the hBN flake, as depicted in Figure 1a.

Figure 2a and b presents the SEM images of the plain nanoslits after patterning with FIB. We use polycarbonate-assisted transfer to place hBN flakes onto the nanoslit array (Figure 2c). We then performed a confocal PL scan of the hBN flake from the frontside (Figure 2d). The scan reveals clear PL enhancement from regions of the hBN flake positioned over the nanoslits, indicating an improved plasmonic enhancement of spin defect emission. This is further confirmed by the PL spectrum taken in Figure 2e, which shows an increase in intensity by a factor of approximately 1.75 compared to hBN on a flat gold film. We found that the plasmonic enhancement achieved using the nanoslit array is strongly dependent on the thickness of the flake. In Figure 2d, while we see PL enhancement on the thinner part of the flakes, we see negligible enhancement on the thicker part of the flake. This experimental observation is in agreement with previous works[19,21,40] as well as COMSOL simulations (Supplementary Figure 2a).

We then proceeded to collect data from the backside of the device by using an oil immersion lens. Figure 3a shows the confocal PL scan from the backside of the device. We observed strong PL emission through the nanoslit array. Upon measuring the PL spectrum of the emission through the nanoslit array, we observed a strong peak centered at 830 nm, confirming that the PL emission is indeed due to V_B^- defects (Figure 3b). If we compare the two PL scans taken at the same 532 nm laser power (2 mW), we collect I_1 from the frontside using the air objective from spot 1 (Figure 2d) and I_2 from the backside using the oil immersion lens. We determine the I_2/I_1 value to be 0.625. This gives us nearly the same PL from V_B^- defects from the backside as plasmonically enhanced defects on plain gold from the frontside.

The clear PL signal from V_B^- defects from the backside allows us to perform continuous wave optically detected magnetic resonance (CW-ODMR) and pulsed measurements (T_1 spin relaxation measurement) from the backside of the device. We measure the ODMR spectrum from the front- and backsides of the device, as shown in Figure 3d. We also

https://doi.org/10.1021/acs.nanolett.6c00108
Nano Lett. 2026, 26, 4410−4417

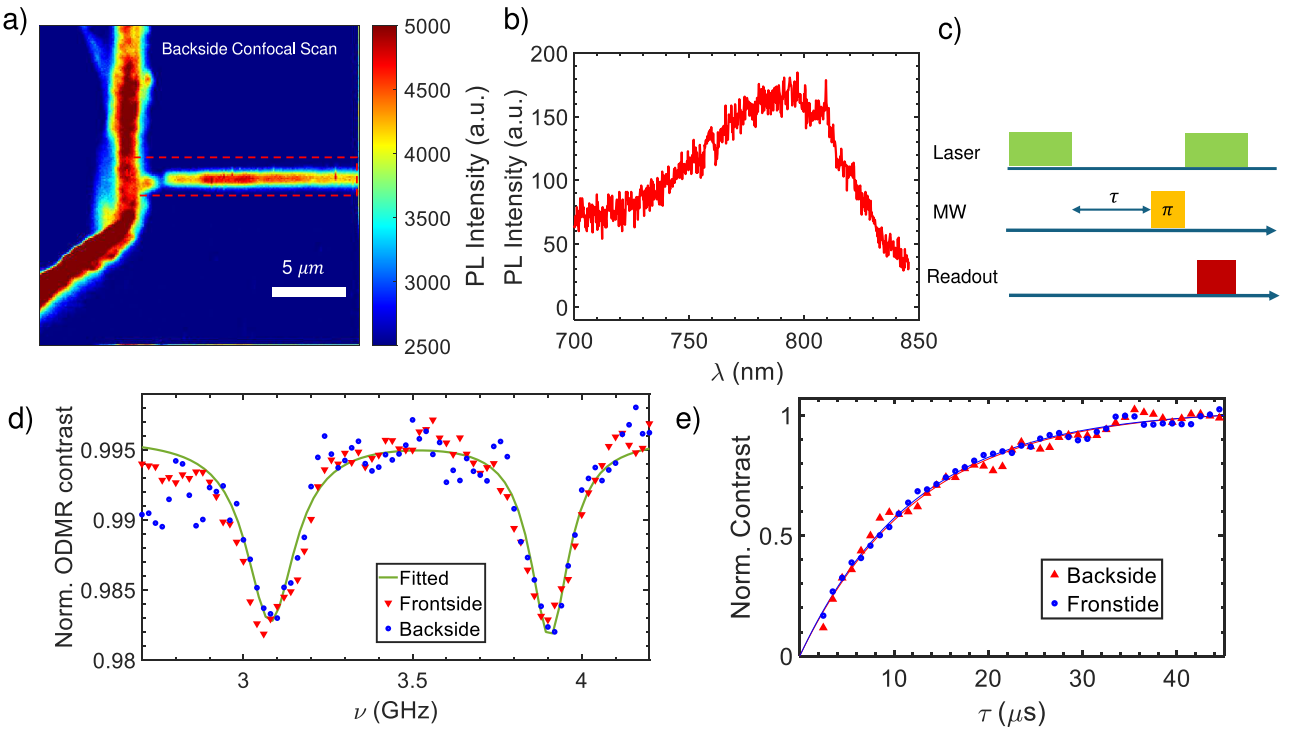

Figure 3. PL, CW-ODMR, and pulsed measurements from the backside of the device. (a) PL confocal scan of the emission from V_B^- defects from the backside using oil immersion lens. The laser power used is 2 mW. (b) PL spectrum from the backside showing a clear peak in the 800−830 nm range, confirming that the emission is indeed from V_B^- defects. The laser power used is 2 mW. (c) Schematic for the pulse sequence for T_1 relaxation time measurement. The defects are first initialized to the $m_s = 0$ state using a laser pulse. The defects are then allowed to evolve for time τ, after which a microwave π pulse is applied to flip the state of the defects from $m_s = 0$ to -1. The final state is then read out by another laser pulse. (d) CW-ODMR from the front- and backsides of the device. Similar contrast shows the consistent performance of the device from the front- and backsides. The microwave power used is 630 mW. (e) T_1 relaxation times from the front- and backsides show good agreement. T_1 time from the front- and backsides was measured to be 12.23 ± 0.44 and 12.57 ± 0.68 μs, respectively.

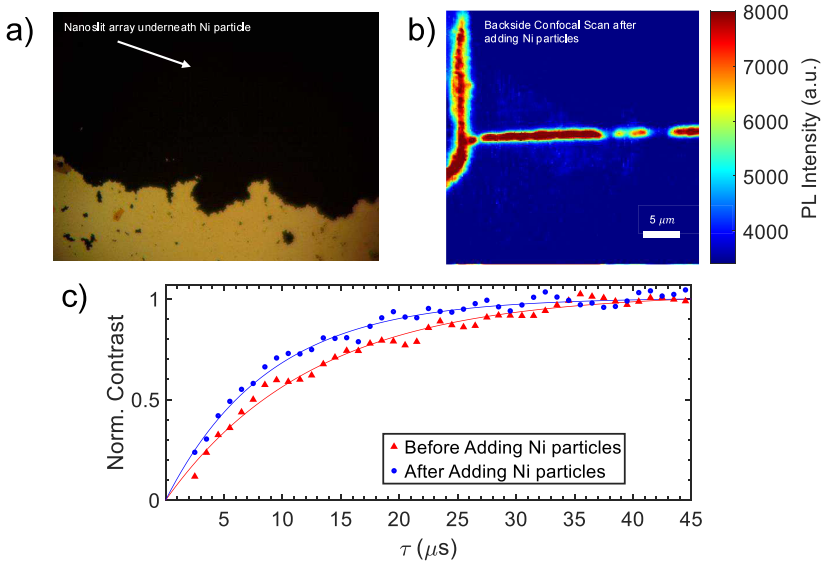

Figure 4. T_1 spin relaxometry measurements to detect spin noise from nickel nanoparticles. (a) Optical image from the frontside of nickel nanoparticles drop casted onto the hBN flake on the nanoslit array. The flake and nanoslit array cannot be seen due to the opaque nature of the nickel nanoparticles. (b) Backside confocal PL scan through the nanoslit array, after dropping nickel nanoparticles on the frontside of the device. We observe clear PL emission through the nanoslit array. The laser power used is 1.8 mW. (c) Reduction in T_1 time due to magnetic spin noise from nickel nanoparticles. We observe a reduction of ∼3.8 μs in the T_1 relaxation time, from 12.57 ± 0.68 to 8.781 ± 0.875 μs, due to the noise generated by nickel nanoparticles.

performed T_1 spin relaxation measurements from the front- and backsides of the device and found both measurements to yield similar results, demonstrating the ability to perform pulsed measurements through this device.

https://doi.org/10.1021/acs.nanolett.6c00108
Nano Lett. 2026, 26, 4410−4417

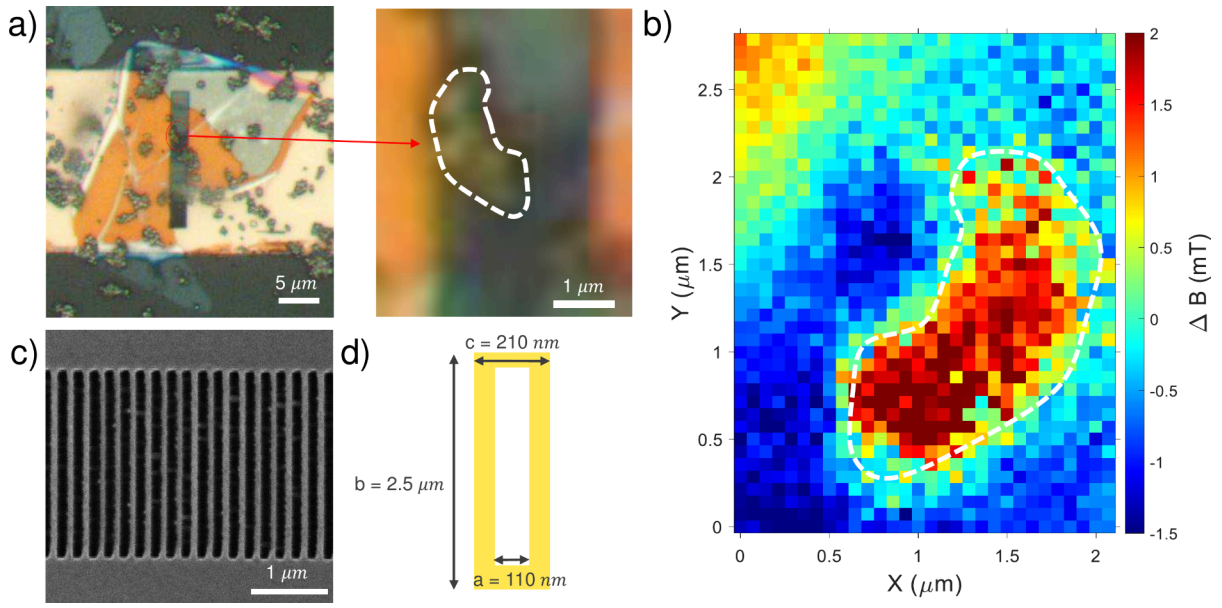

Figure 5. 2D magnetic field mapping of nickel nanoparticles. (a) Optical image of the hBN flake deposited onto the fabricated nanoslit array. A solution of nickel nanoparticles was drop-cast onto the flake, and an isolated cluster was used to perform the 2D magnetic field imaging. (b) 2D magnetic field map of the cluster of nickel nanoparticles. The laser power used is 1.9 mW, and the microwave power used is 200 mW. Each pixel is 71.4 nm. (c) Image of the modified nanoslit array. Imaging is done using a helium FIB, and patterning is done using a neon FIB. (d) Schematic of the modified nanoslit design to perform the 2D magnetic mappping.

To illustrate the sensing capabilities of our device, we performed T_1 relaxometry measurements to detect the influence of magnetic spin noise from nickel nanoparticles on the T_1 relaxation time of V_B^- spin defects. Magnetic spin noise accelerates spin relaxation of V_B^- spin qubits, resulting in a reduced T_1 relaxation time. This technique has previously been used to measure the concentration of Gd^{3+} ions using shallow V_B^- spin qubits.[6,7] However, these approaches face challenges in probing opaque materials because the PL of the spin defects is obstructed from both the front (by the opaque material itself) and the back (by the gold waveguide). Our device overcomes these limitations by enabling T_1 relaxometry using plasmonically enhanced spin defects, allowing us to measure the magnetic spin noise from nickel nanoparticles efficiently.

We drop casted a solution of nickel nanoparticles in acetone onto the frontside of the device. Figure 4a shows the flake being completely covered by the opaque nickel nanoparticles, making any optical measurements from the frontside impossible. Thus, T_1 relaxometry measurements can only be performed by using the backside nanoslit array. Figure 4b shows the PL confocal scan taken from the backside of the device after dropping the nickel nanoparticles. It is evident that we are able to excite and collect emission from V_B^- defects through the nanoslit array from the backside of the device.

We then measured the T_1 spin relaxation time from the backside of the device. We observed a reduction of ~3.8 μs in the T_1 relaxation time, from 12.57 ± 0.68 to 8.781 ± 0.875 μs, after adding nickel nanoparticles. To calculate the spin relaxation induced by the magnetic spin noise from the nickel nanoparticles, we can use the following formula:

$$\Gamma_{\text{nickel}} = \frac{1}{T_{1,\text{nickel}}} - \frac{1}{T_{1,\text{air}}} \quad (1)$$

where $T_{1,\text{air}}$ is the spin relaxation time of the V_B^- spin qubits in the absence of nickel nanoparticles and $T_{1,\text{nickel}}$ is the spin relaxation time measured after adding the nickel nanoparticles. We thus measured Γ_{nickel} to be 34.32 ± 12.13 ms^{-1}.

We then performed 2D magnetic field mapping of a cluster of nickel nanoparticles using our device. To accommodate particles larger than 1 μm in diameter for magnetic imaging, we modified the nanoslit design by increasing the nanoslit length to b = 2.5 μm. Additionally, we widened the nanoslit width (a) and period (c) to simplify the FIB fabrication (Figure 5d) while optimizing the count collection from the backside of the device (Supplementary Figure 1d). We also switched the substrate from silica glass coverslips to sapphire coverslips (100 μm thick) to mitigate mechanical vibrations during the measurement.

A diluted solution of nickel nanoparticles was drop-cast onto a hBN flake, which was deposited on the nanoslit array, as shown in Figure 5a. We then imaged a small, isolated cluster of nanoparticles (Figure 5a) and measured the ODMR spectrum at each pixel to extract the magnetic field shift caused by the nickel nanoparticles. The reference field is calibrated by taking an average of the magnetic field at each pixel in the 2D map, which is 49 mT. The resulting local magnetic field distribution closely matches the shape of the nickel nanoparticle cluster, as indicated by the white outline in Figure 5a and b.

In conclusion, we present a novel waveguide design for the purpose of studying opaque materials using spin qubits in hBN. We use a neon FIB to pattern a nanoslit array onto a very thin gold waveguide and etch through the gold film completely. We observe a PL enhancement of 1.75 times for spin qubits on the nanoslit array compared to plain gold. We observe clear PL from V_B^- spin defects through the nanoslit array, allowing us to perform CW-ODMR and pulsed measurements from the back of the device using an oil immersion lens. Finally, we measure the magnetic spin noise from opaque nickel nanoparticles by measuring the reduction in the T_1 spin relaxation time of the

https://doi.org/10.1021/acs.nanolett.6c00108
Nano Lett. 2026, 26, 4410−4417

V_B^- spin defects from the backside of the device. We also mapped the magnetic field of a cluster of nickel nanoparticles from the backside of the device using the nanoslit array.

Further work can be done to adapt the nanoslit array design to plasmonically enhance single color centers in hBN,[41−46] which have high contrast to further study interesting phenomena in opaque materials. Our work opens new avenues for sensing opaque materials using plasmonically enhanced hBN spin defects. This device architecture holds potential for a broad range of applications, including the *in situ* study of electrochemical processes in lithium-ion batteries as well as chemical and biological sensing in complex or scattering media.

■ ASSOCIATED CONTENT

Supporting Information

The Supporting Information is available free of charge at https://pubs.acs.org/doi/10.1021/acs.nanolett.6c00108.

Details about sample preparation, fabrication of the waveguide, simulations for optical and microwave performance of the coplanar waveguide, and Rabi oscillation data (PDF)

■ AUTHOR INFORMATION

Corresponding Authors

Songtao Wu − *Toyota Research Institute of North America, Ann Arbor, Michigan 48105, United States*; Email: songtao.wu@toyota.com

Tongcang Li − *Department of Physics and Astronomy, Birck Nanotechnology Center, and Purdue Quantum Science and Engineering Institute, Purdue University, West Lafayette, Indiana 47907, United States; Elmore School of Electrical and Computer Engineering, Purdue University, West Lafayette, Indiana 47907, United States;* orcid.org/0000-0003-3308-8718; Email: tcli@purdue.edu

Authors

Saakshi Dikshit − *Elmore School of Electrical and Computer Engineering, Purdue University, West Lafayette, Indiana 47907, United States;* orcid.org/0009-0008-9728-1502

Sumukh Vaidya − *Department of Physics and Astronomy, Purdue University, West Lafayette, Indiana 47907, United States;* orcid.org/0000-0002-9732-6829

Troy Tsubota − *Department of Physics and Astronomy, Purdue University, West Lafayette, Indiana 47907, United States; Department of Physics, University of California, Berkeley, Berkeley, California 94720, United States*

Xingyu Gao − *Department of Physics and Astronomy, Purdue University, West Lafayette, Indiana 47907, United States;* orcid.org/0000-0003-1253-4811

Peng Ju − *Department of Physics and Astronomy, Purdue University, West Lafayette, Indiana 47907, United States;* orcid.org/0000-0002-1128-7858

Zhiyan Xie − *Department of Physics and Astronomy, Purdue University, West Lafayette, Indiana 47907, United States;* orcid.org/0009-0009-3910-7618

Kunhong Shen − *Department of Physics and Astronomy, Purdue University, West Lafayette, Indiana 47907, United States*

Naveed Hussain − *Toyota Research Institute of North America, Ann Arbor, Michigan 48105, United States;* orcid.org/0000-0003-2567-5066

Shougo Higashi − *Toyota Research Institute of North America, Ann Arbor, Michigan 48105, United States*

Debasish Banerjee − *Toyota Research Institute of North America, Ann Arbor, Michigan 48105, United States*

Complete contact information is available at: https://pubs.acs.org/10.1021/acs.nanolett.6c00108

Notes

The authors declare no competing financial interest.

■ ACKNOWLEDGMENTS

The authors thank the Toyota Research Institute of North America for funding this research.

■ REFERENCES

(1) Gottscholl, A.; Kianinia, M.; Soltamov, V.; Orlinskii, S.; Mamin, G.; Bradac, C.; Kasper, C.; Krambrock, K.; Sperlich, A.; Toth, M.; Aharonovich, I.; Dyakonov, V. Initialization and read-out of intrinsic spin defects in a van der Waals crystal at room temperature. *Nature Materials* **2020**, *19*, 540−545.

(2) Vaidya, S.; Gao, X.; Dikshit, S.; Aharonovich, I.; Li, T. Quantum sensing and imaging with spin defects in hexagonal boron nitride. *Advances in Physics: X* **2023**, *8*, 2206049.

(3) Huang, M.; Zhou, J.; Chen, D.; Lu, H.; McLaughlin, N. J.; Li, S.; Alghamdi, M.; Djugba, D.; Shi, J.; Wang, H.; Du, C. R. Wide field imaging of van der Waals ferromagnet Fe_3GeTe_2 by spin defects in hexagonal boron nitride. *Nat. Commun.* **2022**, *13*, 5369.

(4) Healey, A.; Scholten, S.; Yang, T.; Scott, J.; Abrahams, G.; Robertson, I.; Hou, X.; Guo, Y.; Rahman, S.; Lu, Y.; Kianinia, M.; Aharonovich, I.; Tetienne, J. Quantum microscopy with van der Waals heterostructures. *Nat. Phys.* **2023**, *19*, 87−91.

(5) Moon, J. S.; Whitefield, B.; Spencer, L.; Kianinia, M.; Hennessey, M.; Toth, M.; Jeon, W. B.; Kim, J.-H.; Aharonovich, I. Fiber-Integrated van der Waals Quantum Sensor with an Optimal Cavity Interface. *Advanced Optical Materials* **2024**, *12*, 2401987.

(6) Gao, X.; Vaidya, S.; Ju, P.; Dikshit, S.; Shen, K.; Chen, Y. P.; Li, T. Quantum sensing of paramagnetic spins in liquids with spin qubits in hexagonal boron nitride. *ACS Photonics* **2023**, *10*, 2894−2900.

(7) Robertson, I. O.; Scholten, S. C.; Singh, P.; Healey, A. J.; Meneses, F.; Reineck, P.; Abe, H.; Ohshima, T.; Kianinia, M.; Aharonovich, I.; Tetienne, J.-P. Detection of paramagnetic spins with an ultrathin van der Waals quantum sensor. *ACS Nano* **2023**, *17*, 13408−13417.

(8) Yang, T.; Mendelson, N.; Li, C.; Gottscholl, A.; Scott, J.; Kianinia, M.; Dyakonov, V.; Toth, M.; Aharonovich, I. Spin defects in hexagonal boron nitride for strain sensing on nanopillar arrays. *Nanoscale* **2022**, *14*, 5239−5244.

(9) Lyu, X.; Tan, Q.; Wu, L.; Zhang, C.; Zhang, Z.; Mu, Z.; Zúñiga-Pérez, J.; Cai, H.; Gao, W. Strain quantum sensing with spin defects in hexagonal boron nitride. *Nano Lett.* **2022**, *22*, 6553−6559.

(10) Gottscholl, A.; Diez, M.; Soltamov, V.; Kasper, C.; Krauße, D.; Sperlich, A.; Kianinia, M.; Bradac, C.; Aharonovich, I.; Dyakonov, V. Spin defects in hBN as promising temperature, pressure and magnetic field quantum sensors. *Nat. Commun.* **2021**, *12*, 4480.

(11) Liu, W.; Li, Z.-P.; Yang, Y.-Z.; Yu, S.; Meng, Y.; Wang, Z.-A.; Li, Z.-C.; Guo, N.-J.; Yan, F.-F.; Li, Q.; Wang, J.-F.; Xu, J.-S.; Wang, Y.-T.; Tang, J.-S.; Li, C.-F.; Guo, G.-C. Temperature-dependent energy-level shifts of spin defects in hexagonal boron nitride. *ACS Photonics* **2021**, *8*, 1889−1895.

(12) Gao, X.; Vaidya, S.; Li, K.; Ju, P.; Jiang, B.; Xu, Z.; Allcca, A. E. L.; Shen, K.; Taniguchi, T.; Watanabe, K.; Bhave, S. A.; Chen, Y. P.; Ping, Y.; Li, T. Nuclear spin polarization and control in hexagonal boron nitride. *Nat. Mater.* **2022**, *21*, 1024−1028.

(13) Das, S.; Melendez, A. L.; Kao, I.-H.; García-Monge, J. A.; Russell, D.; Li, J.; Watanabe, K.; Taniguchi, T.; Edgar, J. H.; Katoch, J.; Yang, F.; Hammel, P. C.; Singh, S. Quantum sensing of spin

dynamics using boron-vacancy centers in hexagonal boron nitride. *Phys. Rev. Lett.* **2024**, *133*, 166704.
(14) Zhou, J.; Lu, H.; Chen, D.; Huang, M.; Yan, G. Q.; Al-matouq, F.; Chang, J.; Djugba, D.; Jiang, Z.; Wang, H.; Du, C. R. Sensing spin wave excitations by spin defects in few-layer-thick hexagonal boron nitride. *Science Advances* **2024**, *10*, No. eadk8495.
(15) Wang, J.; Ma, F.; Sun, M. Graphene, hexagonal boron nitride, and their heterostructures: properties and applications. *RSC Adv.* **2017**, *7*, 16801−16822.
(16) Yankowitz, M.; Ma, Q.; Jarillo-Herrero, P.; LeRoy, B. J. van der Waals heterostructures combining graphene and hexagonal boron nitride. *Nature Reviews Physics* **2019**, *1*, 112−125.
(17) Zhang, J.; Tan, B.; Zhang, X.; Gao, F.; Hu, Y.; Wang, L.; Duan, X.; Yang, Z.; Hu, P. Atomically thin hexagonal boron nitride and its heterostructures. *Adv. Mater.* **2021**, *33*, 2000769.
(18) Melendez, A. L.; Gong, R.; He, G.; Wang, Y.; Wu, Y.-C.; Poirier, T.; Randolph, S.; Ghosh, S.; Liang, L.; Jesse, S.; Li, A.-P.; Damron, J. T.; Lawrie, B. J.; Edgar, J. H.; Vlassiouk, I. V.; Zu, C.; Zhao, H. Probing boron vacancy defects in hBN via single spin relaxometry. *Nature Communications* **2026**, DOI: 10.1038/s41467-026-70545-6.
(19) Cai, H.; Ru, S.; Jiang, Z.; Eng, J. J. H.; He, R.; Li, F.-l.; Miao, Y.; Zúñiga-Pérez, J.; Gao, W. Spin defects in hBN assisted by metallic nanotrenches for quantum sensing. *Nano Lett.* **2023**, *23*, 4991−4996.
(20) Mendelson, N.; Ritika, R.; Kianinia, M.; Scott, J.; Kim, S.; Fröch, J. E.; Gazzana, C.; Westerhausen, M.; Xiao, L.; Mohajerani, S. S.; Strauf, S.; Toth, M.; Aharonovich, I.; Xu, Z.-Q. Coupling spin defects in a layered material to nanoscale plasmonic cavities. *Adv. Mater.* **2022**, *34*, 2106046.
(21) Xu, X.; Solanki, A. B.; Sychev, D.; Gao, X.; Peana, S.; Baburin, A. S.; Pagadala, K.; Martin, Z. O.; Chowdhury, S. N.; Chen, Y. P.; Taniguchi, T.; Watanabe, K.; Rodionov, I. A.; Kildishev, A. V.; Li, T.; Upadhyaya, P.; Boltasseva, A.; Shalaev, V. M. Greatly enhanced emission from spin defects in hexagonal boron nitride enabled by a low-loss plasmonic nanocavity. *Nano Lett.* **2023**, *23*, 25−33.
(22) Kim, T.; Song, W.; Son, D.-Y.; Ono, L. K.; Qi, Y. Lithium-ion batteries: outlook on present, future, and hybridized technologies. *Journal of Materials Chemistry A* **2019**, *7*, 2942−2964.
(23) Li, M.; Lu, J.; Chen, Z.; Amine, K. 30 years of lithium-ion batteries. *Adv. Mater.* **2018**, *30*, 1800561.
(24) Albero Blanquer, L.; Marchini, F.; Seitz, J. R.; Daher, N.; Bétermier, F.; Huang, J.; Gervillié, C.; Tarascon, J.-M. Optical sensors for operando stress monitoring in lithium-based batteries containing solid-state or liquid electrolytes. *Nat. Commun.* **2022**, *13*, 1153.
(25) Huang, J.; Albero Blanquer, L.; Bonefacino, J.; Logan, E. R.; Alves Dalla Corte, D.; Delacourt, C.; Gallant, B. M.; Boles, S. T.; Dahn, J.; Tam, H.-Y.; Tarascon, J.-M. Operando decoding of chemical and thermal events in commercial Na (Li)-ion cells via optical sensors. *Nature Energy* **2020**, *5*, 674−683.
(26) Han, X.; Zhong, H.; Li, K.; Xue, X.; Wu, W.; Hu, N.; Lu, X.; Huang, J.; Xiao, G.; Mai, Y.; Guo, T. Operando monitoring of dendrite formation in lithium metal batteries via ultrasensitive tilted fiber Bragg grating sensors. *Light: Science & Applications* **2024**, *13*, 24.
(27) Nascimento, M.; Novais, S.; Ding, M. S.; Ferreira, M. S.; Koch, S.; Passerini, S.; Pinto, J. L. Internal strain and temperature discrimination with optical fiber hybrid sensors in Li-ion batteries. *J. Power Sources* **2019**, *410*, 1−9.
(28) Cheng, X.; Pecht, M. In Situ Stress Measurement Techniques on Li-ion Battery Electrodes: A Review. *Energies* **2017**, *10*, 591.
(29) Sethuraman, V. A.; Srinivasan, V.; Bower, A. F.; Guduru, P. R. In situ measurements of stress-potential coupling in lithiated silicon. *J. Electrochem. Soc.* **2010**, *157*, A1253−1261.
(30) Sethuraman, V. A.; Chon, M. J.; Shimshak, M.; Srinivasan, V.; Guduru, P. R. In situ measurements of stress evolution in silicon thin films during electrochemical lithiation and delithiation. *J. Power Sources* **2010**, *195*, 5062−5066.
(31) Hatano, Y.; Shin, J.; Tanigawa, J.; Shigenobu, Y.; Nakazono, A.; Sekiguchi, T.; Onoda, S.; Ohshima, T.; Arai, K.; Iwasaki, T.; Hatano, M. High-precision robust monitoring of charge/discharge current over a wide dynamic range for electric vehicle batteries using diamond quantum sensors. *Sci. Rep.* **2022**, *12*, 13991.
(32) Hatano, Y.; Tanigawa, J.; Nakazono, A.; Sekiguchi, T.; Onoda, S.; Ohshima, T.; Iwasaki, T.; Hatano, M. A wide dynamic range diamond quantum sensor as an electric vehicle battery monitor. *Philosophical Transactions of the Royal Society A* **2024**, *382*, 20220312.
(33) Kubota, K.; Hatano, Y.; Kainuma, Y.; Shin, J.; Nishitani, D.; Shinei, C.; Taniguchi, T.; Teraji, T.; Onoda, S.; Ohshima, T.; Iwasaki, T.; Hatano, M. Wide temperature operation of diamond quantum sensor for electric vehicle battery monitoring. *Diamond Relat. Mater.* **2023**, *135*, 109853.
(34) Liu, B.; Chen, X.-Q.; Shang, Y.-X.; Xiong, X.; Zheng, H.; Liu, G.-Q.; Suo, L. Operando quantum sensing captures the nanoscale electrochemical evolution in batteries. *Device* **2024**, *2*, 100521.
(35) Scholten, S. C.; Iwański, J.; Xing, K.; Binder, J.; Dąbrowska, A. K.; Tan, H. H.; Cheng, T. S.; Bradford, J.; Mellor, C. J.; Beton, P. H.; Novikov, S. V.; Krotkus, S.; Mischke, J.; Yengel, E.; Henning, A.; Pasko, S.; Wysmołek, A.; Tetienne, J.-P. Optically detected magnetic resonance of wafer-scale hexagonal boron nitride thin films. *Materials for Quantum Technology* **2025**, *5*, 045701.
(36) Ivády, V.; Barcza, G.; Thiering, G.; Li, S.; Hamdi, H.; Chou, J.-P.; Legeza, Ö.; Gali, A. Ab initio theory of the negatively charged boron vacancy qubit in hexagonal boron nitride. *npj Computational Materials* **2020**, *6*, 41.
(37) Mu, Z.; Cai, H.; Chen, D.; Kenny, J.; Jiang, Z.; Ru, S.; Lyu, X.; Koh, T. S.; Liu, X.; Aharonovich, I.; Gao, W. Excited-state optically detected magnetic resonance of spin defects in hexagonal boron nitride. *Phys. Rev. Lett.* **2022**, *128*, 216402.
(38) Baber, S.; Malein, R. N. E.; Khatri, P.; Keatley, P. S.; Guo, S.; Withers, F.; Ramsay, A. J.; Luxmoore, I. J. Excited state spectroscopy of boron vacancy defects in hexagonal boron nitride using time-resolved optically detected magnetic resonance. *Nano Lett.* **2022**, *22*, 461−467.
(39) Mathur, N.; Mukherjee, A.; Gao, X.; Luo, J.; McCullian, B. A.; Li, T.; Vamivakas, A. N.; Fuchs, G. D. Excited-state spin-resonance spectroscopy of V_B^- defect centers in hexagonal boron nitride. *Nat. Commun.* **2022**, *13*, 3233.
(40) Gao, X.; Jiang, B.; Llacsahuanga Allcca, A. E.; Shen, K.; Sadi, M. A.; Solanki, A. B.; Ju, P.; Xu, Z.; Upadhyaya, P.; Chen, Y. P.; Bhave, S. A.; Li, T. High-contrast plasmonic-enhanced shallow spin defects in hexagonal boron nitride for quantum sensing. *Nano Lett.* **2021**, *21*, 7708−7714.
(41) Gao, X.; Vaidya, S.; Li, K.; Ge, Z.; Dikshit, S.; Zhang, S.; Ju, P.; Shen, K.; Jin, Y.; Ping, Y.; Li, T. Single nuclear spin detection and control in a van der Waals material. *Nature* **2025**, *643*, 943−949.
(42) Stern, H. L.; Gu, Q.; Jarman, J.; Eizagirre Barker, S.; Mendelson, N.; Chugh, D.; Schott, S.; Tan, H. H.; Sirringhaus, H.; Aharonovich, I.; Atatüre, M. Room-temperature optically detected magnetic resonance of single defects in hexagonal boron nitride. *Nat. Commun.* **2022**, *13*, 618.
(43) Chejanovsky, N.; Mukherjee, A.; Geng, J.; Chen, Y.-C.; Kim, Y.; Denisenko, A.; Finkler, A.; Taniguchi, T.; Watanabe, K.; Dasari, D. B. R.; Auburger, P.; Gali, A.; Smet, J. H.; Wrachtrup, J. Single-spin resonance in a van der Waals embedded paramagnetic defect. *Nature Materials* **2021**, *20*, 1079−1084.
(44) Guo, N.-J.; Li, S.; Liu, W.; Yang, Y.-Z.; Zeng, X.-D.; Yu, S.; Meng, Y.; Li, Z.-P.; Wang, Z.-A.; Xie, L.-K.; Ge, R.-C.; Wang, J.-F.; Li, Q.; Xu, J.-S.; Wang, Y.-T.; Tang, J.-S.; Gali, A.; Li, C.-F.; Guo, G.-C. Coherent control of an ultrabright single spin in hexagonal boron nitride at room temperature. *Nat. Commun.* **2023**, *14*, 2893.
(45) Stern, H. L.; Gilardoni, C. M.; Gu, Q.; Eizagirre Barker, S.; Powell, O. F.; Deng, X.; Fraser, S. A.; Follet, L.; Li, C.; Ramsay, A. J.; Tan, H. H.; Aharonovich, I.; Atatüre, M. A quantum coherent spin in hexagonal boron nitride at ambient conditions. *Nat. Mater.* **2024**, *23*, 1379−1385.
(46) Mendelson, N.; Chugh, D.; Reimers, J. R.; Cheng, T. S.; Gottscholl, A.; Long, H.; Mellor, C. J.; Zettl, A.; Dyakonov, V.; Beton, P. H.; Novikov, S. V.; Jagadish, C.; Tan, H. H.; Ford, M. J.; Toth, M.; Bradac, C.; Aharonovich, I. Identifying carbon as the source of visible

single-photon emission from hexagonal boron nitride. *Nature Materials* **2021**, *20*, 321−328.

https://doi.org/10.1021/acs.nanolett.6c00108
Nano Lett. 2026, 26, 4410−4417